



Effects of vessel wall mechanics on non-invasive evaluation of cardiovascular intrinsic frequencies

Arian Aghilinejad^{a,1}, Rashid Alavi^{a,1}, Bryson Rogers^a, Faisal Amlani^a, Niema M. Pahlevan^{a,b,*}

^a Department of Aerospace & Mechanical Engineering, University of Southern California, Los Angeles, USA

^b Division of Cardiovascular Medicine, Department of Medicine, Keck School of Medicine, University of Southern California, Los Angeles, USA

ARTICLE INFO

Keywords:

Pulse wave analysis
Cardiovascular intrinsic frequency
Non-invasive measurement
Fluid-structure interaction
Hemodynamic

ABSTRACT

Intrinsic Frequency (IF) is a systems-based approach that provides valuable information for hemodynamic monitoring of the left ventricle (LV), the arterial system, and their coupling. Recent clinical studies have demonstrated the clinical significance of this method for prognosis and diagnosis of cardiovascular diseases. In IF analysis, two dominant instantaneous frequencies (ω_1 and ω_2) are extracted from arterial pressure waveforms. The value of ω_1 is related to the dynamics of the LV and the value of ω_2 is related to the dynamics of vascular function. This work investigates the effects of vessel wall mechanics on the accuracy and applicability of IFs extracted from vessel wall displacement waveforms compared to IFs extracted from pressure waveforms. In this study, we used a computational approach employing a fluid–structure interaction finite element method for various wall mechanics governed by linearly elastic, hyperelastic, and viscoelastic models. Results show that for vessels with elastic wall behavior, the error between displacement-based and pressure-based IFs is negligible. In the presence of stenosis or aneurysm in elastic arteries, the maximum errors associated with displacement-based IFs is less than 2%. For non-linear elastic and viscoelastic arteries, errors are more pronounced (where the former reaches up to 11% and the latter up to 27%). Our results ultimately suggest that displacement-based computations of ω_1 and ω_2 are accurate in vessels that exhibit elastic behavior (such as carotid arteries) and are suitable surrogates for pressure-based IFs. This is clinically significant because displacement-based IFs can be measured non-invasively.

1. Introduction

The Intrinsic Frequency (IF) method (Alavi et al., 2021; Pahlevan et al., 2014; Tavallali et al., 2015) is a novel systems-based approach for hemodynamic monitoring of the left ventricle (LV), arterial system, and their coupling. In previous studies, IFs and their associated parameters have been shown to provide clinically-valuable information for health assessment as well as diagnosis of cardiovascular-related diseases (Cooper et al.; Mogadam et al., 2020; Tavallali et al., 2018). Based on a sparse time–frequency representation for nonlinear and nonstationary signals, the IF method extracts, from central waveforms, the dominant instantaneous frequencies in each of the two major (systolic and diastolic) phases of a cardiac cycle. The first IF, ω_1 , is linked to the systolic phase and related to LV function (Pahlevan et al., 2017). The second IF, ω_2 , is linked to the diastolic phase (after closure of the aortic valve) and related to the afterload or vascular function (Mogadam et al., 2020;

Tavallali et al., 2015; Tavallali et al., 2018). The clinical relevancy of intrinsic frequencies (and other IF parameters, e.g., the difference in ω_1 and ω_2 , or corresponding wave envelopes) in the assessment of cardiovascular health and detection of diseased conditions has been established in both humans and small animals (Alavi et al., 2019, 2020; Cooper, et al.; Miller et al., 2020; Mogadam et al., 2020; Pahlevan et al., 2020; Pahlevan and Matthews, 2019; Pahlevan et al., 2017; Petrusek et al., 2015). For example, in a clinical study, Mogadam et al. (Mogadam et al., 2020) have demonstrated that the IF method is useful in evaluating LV hemodynamics following transcatheter aortic valve replacement (TAVR). More recently, Cooper et al. (Cooper, et al.) have shown that IF parameters derived from single central carotid waveforms are predictive of heart failure in the large Framingham Heart Study cohort, potentially representing valuable new biomarkers for cardiovascular disease outcomes in the community.

A substantial advantage of the IF method is that only one arterial

* Corresponding author at: Room 470, Michelson Building (MCB), 1002 Childs Way, Los Angeles CA 90089, USA.

E-mail address: pahlevan@usc.edu (N.M. Pahlevan).

¹ These authors contributed equally.

pressure waveform is required to extract IF parameters and perform the analysis, whereas both pressure and flow measurements are required by many well-established wave analysis techniques (e.g., the impedance method, pulse wave analysis, wave intensity (WI), and wave power analysis) (Aghilinejad et al., 2021; Kang et al., 2019; Mynard and Smolich, 2016; Parker, 2009). Additionally, IFs can be extracted from any raw pressure signal, without regards to absolute values and units; therefore, the need for system calibration is obviated (Pahlevan et al., 2017). As such, the IF method can be applied to any waveform signal, including those acquired inexpensively, easily and non-invasively (such as via handheld devices (Rinderknecht et al., 2020) or iPhones (Pahlevan et al., 2017)) through measurements of vessel wall displacements (i.e., diameter changes) of central arteries. Previous studies, mostly related to large blood vessels such as the aorta (where viscoelastic effects can be assumed as negligible), have demonstrated morphological similarities between the displacement and pressure waveforms (including phase) (Young and Tsai, 1973). However, non-linear characteristics of some vessel wall motions have been shown to result in energy losses due to viscosity changes that may arise under diseased conditions such as hypertension (Simon and Levenson, 2001; Stefanadis et al., 1997). In distal arteries (where this degree of nonlinearity and viscoelasticity may be significant (Reymond et al., 2009)), the accuracy of the (non-invasive) displacement-based IF method is unknown.

Our aim in this study is to comprehensively investigate, under various assumptions of vessel wall mechanics and geometrical configurations, the feasibility of using wall displacement as a surrogate for pressure in extracting IFs. We performed computational fluid–structure interaction (FSI) modeling for pressure waves and vessel wall displacement considering different vessel wall mechanics such as linear elasticity, nonlinear elasticity (hyperelasticity) and viscoelasticity (Gasser et al., 2006). We considered cases with different levels of viscoelastic behavior, from little to none (e.g., the behavior of large central arteries such as the aorta or the carotid artery) as well as significant levels (e.g., the behavior of small and muscular arteries). We additionally examined the accuracy of displacement-based IFs in the presence of geometrical configurations representing effects of certain cardiovascular diseases such as aneurysms and stenosis.

2. Materials and methods

2.1. The intrinsic frequency (IF) method

In the IF method, it is assumed that the instantaneous frequencies are piecewise constant throughout the cardiac cycle with a jump at the time of decoupling (e.g., the aortic notch) (Tavallali et al., 2015). In essence, for an arterial pressure waveform (P), the IF problem is formulated as

$$P(a_i, b_i, \omega_i, c; t) = (a_1 \cos \omega_1 t + b_1 \sin \omega_1 t) \chi_{[0, T_0)}(t) + (a_2 \cos \omega_2 t + b_2 \sin \omega_2 t) \chi_{[T_0, T)}(t) + c \quad (1)$$

where

$$a_1^p \cos(\omega_1^p t) + b_1^p \sin(\omega_1^p t) - \tau_\epsilon a_1^p \omega_1^p \sin(\omega_1^p t) + \tau_\sigma b_1^p \omega_1^p \cos(\omega_1^p t) = E_R a_1^u \cos(\omega_1^u t) + E_R b_1^u \sin(\omega_1^u t) - E_R \tau_\sigma a_1^u \omega_1^u \sin(\omega_1^u t) + E_R \tau_\sigma b_1^u \omega_1^u \cos(\omega_1^u t) \quad (6)$$

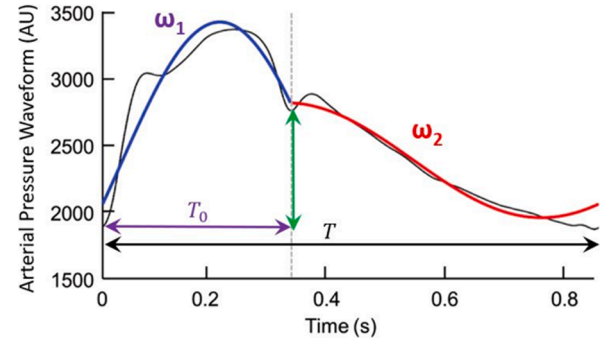


Fig. 1. Schematic of the Intrinsic Frequency (IF) reconstruction of an arterial waveform. The original raw pressure waveform (black) in an arbitrary unit (AU) overlaid on top of the reconstructed waveform (blue and red) using the IF method. This results in a five-dimensional space (IF space) consisting of ω_1 , ω_2 , T_0 , T , and the relative height of decoupling at the aortic notch ($RHDN$; the green arrow divided by the total range). The location of the aortic notch is marked by the vertical gray dotted line. (For interpretation of the references to colour in this figure legend, the reader is referred to the web version of this article.)

are the first and second intrinsic frequencies; and c is a translation constant for the whole period $[0, T]$, where T is the length of the cardiac cycle. In order to find the IF parameters from Eq. (1), an L^2 minimization problem is solved. This minimization problem is subjected to two constraints of ensuring continuity at a time $t = T_0$ (corresponding to the aortic notch) and ensuring periodicity at $t = T$. Fig. 1 shows how accurately the IF-reconstructed waveform represents the original waveform.

2.2. Theoretical analysis of Displacement-Based IFs in linear viscoelastic solids

The constitutive relationship between vessel wall displacement \hat{u} and pressure (stress) \hat{P} using a linear solid viscoelastic model is given by

$$\hat{P} + \tau_\epsilon \dot{\hat{P}} = E_R (\hat{u} + \tau_\sigma \dot{\hat{u}}) \quad (3)$$

where τ_ϵ , τ_σ , and E_R are material constants. These constants can be expressed in terms of spring-dashpot parameters (spring constants k_0 , k_1 and damping coefficient c_1) related to a standard solid viscoelastic model, i.e., $\tau_\epsilon = c_1/k_1$, $\tau_\sigma = c_1(k_1 + k_0)/k_0 k_1$ and $E_R = k_0$. As stated in the previous section, in the range of $[0, T_0)$, the IF-reconstructed waveform approximations of pressure \hat{P} and displacement \hat{u} are given by

$$\hat{P} = a_1^p \cos(\omega_1^p t) + b_1^p \sin(\omega_1^p t) \quad (4)$$

$$\hat{u} = a_1^u \cos(\omega_1^u t) + b_1^u \sin(\omega_1^u t) \quad (5)$$

where a_1^p and b_1^p are pressure-based envelopes; a_1^u and b_1^u are displacement-based envelopes; and ω_1^p and ω_1^u are the first IFs corresponding to the pressure and displacement waveforms, respectively. Substituting Eq. (4) and Eq. (5) into Eq. (3) yields

Since the first portion of the pressure and displacement waveforms (during systole) are much closer to the shape of an incomplete sine wave (rather than a cosine wave), we can assume $a_1^p \ll b_1^p$ and $a_1^u \ll b_1^u$ during

$$\chi_{(\alpha, \beta)}(t) = \begin{cases} 1, & \alpha \leq t < \beta \\ 0, & \text{otherwise} \end{cases} \quad (2)$$

In Eq. (1) and (2), a_1 , b_1 , a_2 , and b_2 are constant coefficients; ω_1 and ω_2

the $[0, T_0)$ time interval. Hence, without loss of generality, we can neglect the α_1^p and α_1^u terms to produce the expression

$$b_1^p \sin(\omega_1^p t) + \tau_e b_1^p \omega_1^p \cos(\omega_1^p t) = E_R b_1^u \sin(\omega_1^u t) + E_R \tau_e b_1^u \omega_1^u \cos(\omega_1^u t) \quad (7)$$

Note that in the absence of viscoelasticity, $\tau_e = \tau_\sigma = 0$, resulting in $\omega_1^p = \omega_1^u$ (i.e., the IFs are the same, as expected) and $b_1^p = E_R b_1^u$.

In the presence of the viscoelasticity, Eq. (7) must hold for all t in the range of $[0, T_0)$. At $t = 0$, the relationship between ω_1^p and ω_1^u can be derived as

$$\omega_1^p = \frac{\tau_e E_R b_1^u}{\tau_e b_1^p} \omega_1^u \quad (8)$$

In the standard solid viscoelastic model (Lin, 2020), the relationship

between the relaxation time constant τ_e and the creep time constant τ_σ is given by

$$\tau_e = (1 - g) \tau_\sigma \quad (9)$$

where $g = k_1/(k_1 + k_0)$ is a dimensionless parameter depending on material properties. Substituting Eq. (9) into Eq. (8) and re-arranging results in

$$\frac{\omega_1^p}{\omega_1^u} = \frac{1}{(1 - g)} \frac{E_R b_1^u}{b_1^p} \quad (10)$$

Here, $g \in (0, 1)$ can be physically interpreted as a parameter governing the degree of viscoelasticity in the material. In the case of $g \ll 1$, the vessel wall behaves more like an elastic material and we have that

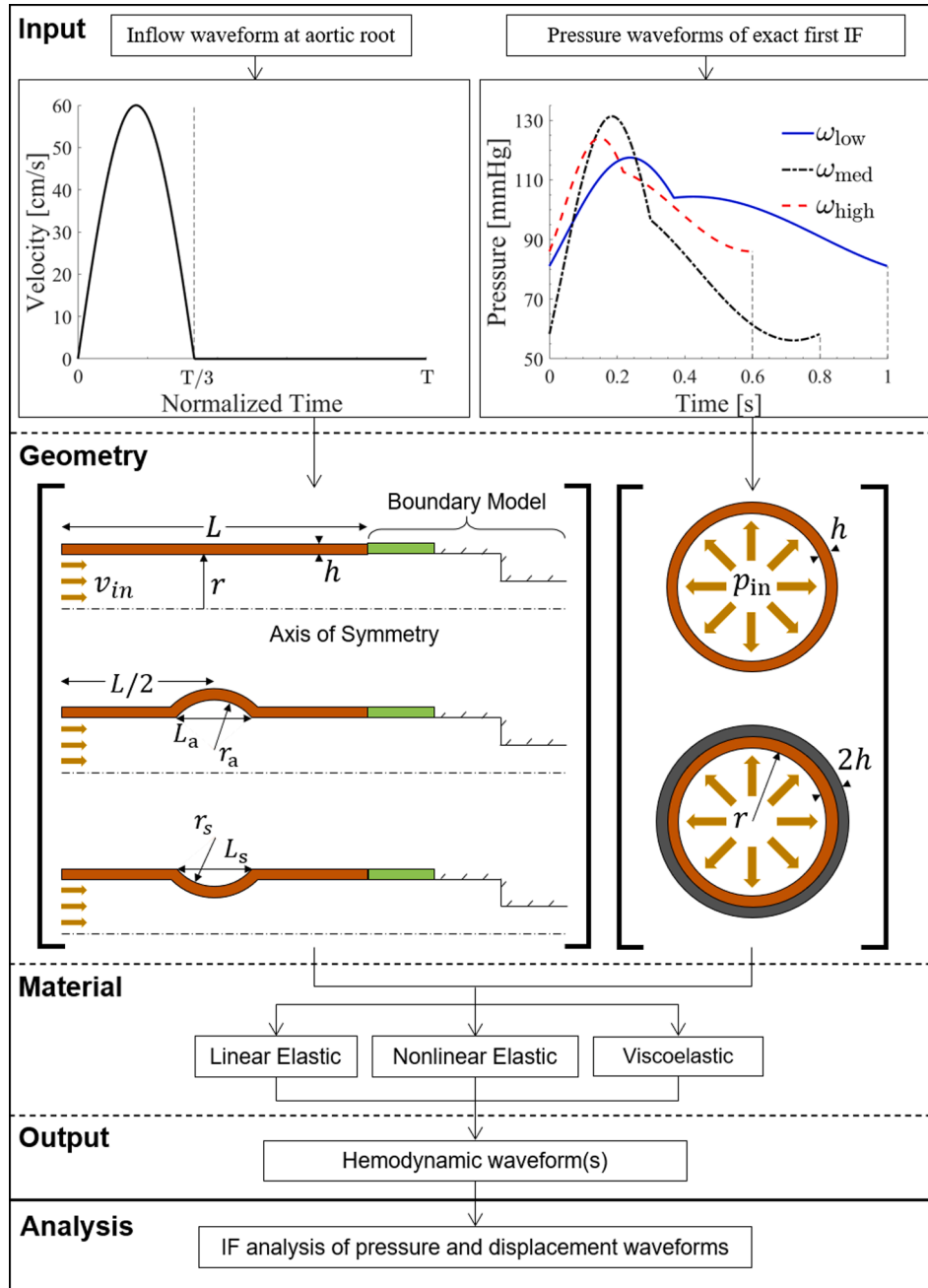


Fig. 2. Flow chart summary of the methodology. A velocity waveform is applied to the inlet of either straight, aneurysmal, or stenotic finite axisymmetric models. Pressure waveforms, reconstructed from exact pressure-based IFs, are applied to both single- and double-layer infinite tube models. Three materials are considered for each model: linear elastic, nonlinear elastic and viscoelastic. IFs are then extracted from the output waveforms.

$\frac{\omega_1^p}{\omega_1^u} \approx 1$ from Eq. (10) (recall that $b_1^p = E_R b_1^u$ for the elastic case). As the value of g grows, the vessel wall becomes more viscous and behaves like a viscoelastic material (Lin, 2020); hence the ratio (disagreement) increases between the pressure-based and displacement-based IFs. In its limit (g close to 1), the vessel wall does not respond at all, yielding $\omega_1^u \rightarrow 0$. Recall that we have assumed in this analysis that $a_1^p \ll b_1^p$ and $a_1^u \ll b_1^u$, which has allowed us to neglect the cosine contributions of the IF wave representations. Hence, it can be reasonably assumed that the actual error between the displacement-based ω_1^u and pressure-based ω_1^p will behave nonlinearly (hence the motivation and use of numerical simulations in the present work). A similar analysis can be performed during the diastolic phase, demonstrating similar behavior between ω_2^p and ω_2^u .

2.3. Physical and computational model

A finite element solver (see Appendix A for details) was used to assess the applicability of displacement-based IFs. Two different vessel wall models were considered (Fig. 2): a flow-sourced “finite axisymmetric” tube and a pressure-sourced “infinite tube”. The infinite tube model was used to investigate the agreement of computed displacement-based IFs with exact applied pressure-based IFs, and the finite axisymmetric tube model was used to investigate the agreement of computed displacement-based and pressure-based IFs in the presence of irregular vessel geometries that mimic aneurysm and stenosis. The finite model assumed an axisymmetric geometry where the deformable fluid and solid domains were strongly coupled and connected to an outflow boundary model (Fig. 2) (Pahlevan et al., 2011; Pahlevan and Gharib, 2011). In this flow-sourced model, a sinusoidal inflow boundary condition with a flat velocity profile and a 1/3 ejection cycle was applied to the vessel inlet (Aghilinejad et al., 2020). Three different geometries were simulated: a straight tube (regular, healthy), a bulged tube (irregular, aneurysm), and a tube with contraction (irregular, stenosis). The second vessel wall model (pressure-sourced) considered the domain as an infinite tube with a boundary of deformable 2D solid elements (i.e.,

an annulus, see Fig. 2). Pressure waveforms corresponding to low, medium, and high values of the first intrinsic frequency ω_1 were applied to the inner surface of vessel wall (based on the available clinical data (Liu and Pahlevan, 2021)). Two different infinite tube geometries were simulated: single- and double-layered to investigate nonlinear elastic behavior (hyperelasticity). Although blood vessels have three layers in reality (from inner to outer: intima, media, and adventitia), the intima is known to be very thin and hence is often lumped together with the media into a single layer (Payne, 2004). The inputs, geometries, material assumptions, and outputs of the computational models are summarized in Fig. 2. The corresponding geometric parameters in all cases are provided in Table 1.

Three vessel wall material types were simulated for both the finite axisymmetric and infinite tube models: linear elastic, nonlinear elastic, and viscoelastic. The linear and nonlinear elastic material assumptions correspond to large central arteries, such as the aorta or carotid artery, whereas the viscoelastic material assumptions correspond to the small, muscular arteries located distal to the left ventricle (Gasser et al., 2006). Wall viscosities of 3000, 6000, and 9000 Pa·s were used in accordance with previous studies in order to cover the whole range of expected physiological behavior (Wang et al., 2015; Warriner et al., 2008). Blood was assumed to be an incompressible and Newtonian fluid (Table 1).

2.4. Governing equations

Details on the overall fluid–structure governing equations are presented in Appendix B. We present in what follows a description of the elastic, non-linear elastic and viscoelastic models.

2.4.1. Modeling linear and nonlinear elasticity

The nonlinear elastic material parameters were determined using the strain-energy function ψ of a modified Veronda-Westmann constitutive model of a nonlinear elastic material (Martins et al., 2006). The general form of this function is given by

$$\psi = D_1 \left[e^{D_2 (\bar{I}_1 - 3)} - 1 \right] + C_2 (\bar{I}_2 - 3) + E_1 (I_3^{1/2} - 1)^2 \quad (11)$$

where $I_3 = \det(\mathcal{C})$ is the third invariant of the right Cauchy-Green tensor \mathcal{C} ; $\bar{I}_1 = I_1 I_3^{-1/3}$ is the reduced first invariant with $I_1 = \text{tr}(\mathcal{C})$; $\bar{I}_2 = I_2 I_3^{-2/3}$ is the reduced second invariant with $I_2 = 1/2 [\text{tr}(\mathcal{C})^2 - \text{tr}(\mathcal{C}^2)]$; and D_1 , D_2 , C_2 , and E_1 are constants determined by material behavior (Fung, 2013). The latter set of material constants are obtained by fitting Eq. (11) to experimental stress-stretch measurements acquired from uniaxial tensile tests of media and adventitia performed by Holzapfel et al. (Holzapfel et al., 2005). Fig. 3a and 3b present the corresponding data and fitted functions.

2.4.2. Modeling viscoelasticity

The standard solid viscoelastic representation (also known as the generalized Maxwell representation) consists of one linear spring k_0 in parallel with n branches that each contain one linear spring k_i and one viscous dashpot (damper) c_i in series, as illustrated in Fig. 3c (Lin, 2020). This model can be simplified to a one-term Maxwell model, illustrated in Fig. 3d, which has been used in the theoretical discussion. The relationship between the deviatoric stress tensor S and shear modulus G as well as the relationship between normal stress σ and bulk modulus K are described respectively by

$$S_{ij}(t) = 2G(0)e_{ij}(t) + 2 \int_0^t e_{ij}(t-\tau) \frac{dG(\tau)}{d\tau} d\tau, \quad (12)$$

$$\sigma_{kk}(t) = 3K(0)\varepsilon_{kk}(t) + 3 \int_0^t \varepsilon_{kk}(t-\tau) \frac{dK(\tau)}{d\tau} d\tau, \quad (13)$$

where t is time; $S_{ij} = T_{ij} - \frac{1}{3}\delta_{ij}T_{kk}$ is the deviatoric stress in terms of

Table 1

Geometric and material parameters used in the computational models.

Name	Variable	Value	Unit
Length of the aortic model	L	20	cm
Inner Radius of the aortic model	r	1	cm
Thickness of the aortic model	h	0.1	cm
Radius of the stenotic bulge	r_s	1.55	cm
Length of the stenotic bulge	L_s	2.00	cm
Radius of the aneurysmal bulge	r_a	1.87	cm
Length of the aneurysmal bulge	L_a	3.20	cm
Viscosity of the Fluid	μ	0.005	Pa·s
Density of the Fluid, Solid	ρ_f, ρ_s	1.05	g/cm ³
Poisson ratio of the aortic wall	θ	0.45	–
Young's Modulus of Elastic wall	E	100	KPa
Viscoelastic Wall Parameters (Prony Series Coefficients)			
Wall Viscosity of 3000 Pa·s	(G_∞, G_1, G_2)	(87, 497, 8)	KPa
	(β_1, β_2)	(100, 10)	s
Wall Viscosity of 6000 Pa·s	(G_∞, G_1, G_2)	(87, 744, 64)	KPa
	(β_1, β_2)	(100, 10)	s
Wall Viscosity of 9000 Pa·s	(G_∞, G_1, G_2)	(91, 971, 127)	KPa
	(β_1, β_2)	(100, 10)	s

* Values of wall viscosities have been adopted in order to capture the full physiological range as reported in literature (Wang et al., 2015; Warriner et al., 2008). The value of blood viscosity has been adopted from other cardiovascular studies (Pahlevan and Gharib, 2011; Kang et al., 2019).

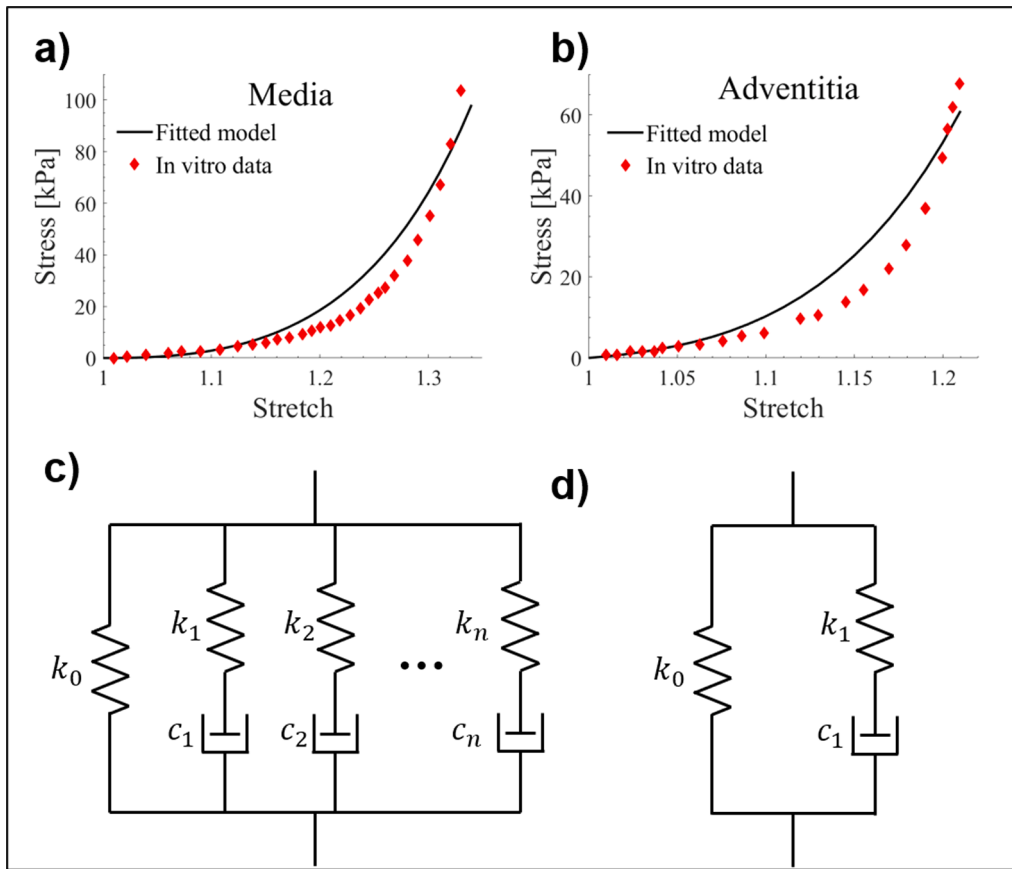


Fig. 3. Material configurations for the vessel wall. In-vitro stress-stretch measurements and corresponding curve-fitting used for determining nonlinear elastic material parameters of the (a) media and (b) adventitia (Holzapfel et al., 2005). (c) The standard solid viscoelastic representation and (d) the single-term Maxwell representation of viscoelasticity.

components T_{ij} of the stress tensor; δ_{ij} is the Kronecker delta; and $e_{ij} = \varepsilon_{ij} - \frac{1}{3}\delta_{ij}\varepsilon_{kk}$ is deviatoric strain in terms of components ε_{ij} of the strain tensor (Amabili et al., 2018; Holzapfel et al., 2002). The functions $G(t)$ and $K(t)$ can be expressed as two-term Prony series (relaxation functions composed of exponential series) given by

$$G(t) = G_{\infty} + \sum_{i=1}^2 G_i e^{-\beta_i t} \quad (14)$$

$$K(t) = K_{\infty} + \sum_{i=1}^2 K_i e^{-\gamma_i t} \quad (15)$$

where G_{∞} and K_{∞} are the long-term shear and bulk moduli; G_i and K_i are the coefficients of the i^{th} time-dependent terms of the shear and bulk moduli; and β_i and γ_i are the decay time constants of the i^{th} time-dependent terms of the shear and bulk moduli, respectively (Table 1). The parameters corresponding to the Prony series representation of the shear modulus (Eq. (14)) was adopted from values reported by Wang et al. (Wang et al., 2015), and the bulk modulus was chosen to satisfy the common assumption that it is orders-of-magnitude larger than the shear modulus, i.e. $K \gg G$ (Qiu and Li, 2019).

3. Results

3.1. Infinite tube model with exact Pressure-based IFs

Fig. 4 presents the displacement waveforms for elastic and viscoelastic cases (with different wall viscosities) of the infinite tube model employing three different pressure waveforms with exact IF parameters. The pressure and displacements are normalized by the maximum amplitude.

Table 2 presents values of ω_1 and ω_2 calculated from the displacement waveforms corresponding to each infinite tube case. For comparison, the known IFs of the input pressure waveforms are provided as well. The normalized displacement waveforms are identical to the input pressure waveforms of the elastic infinite tube model. For the non-linear elastic model, there are marginal differences between the pressure-based and displacement-based IFs. For the viscoelastic model, as the degree of viscoelasticity increases, there is a phase difference between the displacement and pressure waveforms (Fig. 4d-f). Such phase differences result in deviations between the displacement-based and pressure-based IF parameters as shown in Table 2.

3.2. Straight vessel model

Table 3 presents values of ω_1 and ω_2 extracted from the displacement and pressure waveforms at the same location produced by the elastic, hyperelastic, and viscoelastic cases of the pulsatile flow in a regular axisymmetric vessel model. The relative error is defined as $\frac{|\omega_i^{\text{press}} - \omega_i^{\text{disp}}|}{\omega_i^{\text{press}}}$, where ω_i^{press} and ω_i^{disp} are pressure-based and displacement-based IFs, respectively ($i = 1, 2$).

3.3. Aneurysmal and stenotic vessel models

For the aneurysmal model, Fig. 5 presents the fluid velocity amplitudes (overlaid with the corresponding streamlines) and the pressure distributions in the fluid domain, the contour plots for displacement amplitudes in the solid domain at various snapshots in time during a cardiac cycle of length T , as well as the pressure and vessel wall displacement waveforms. Fig. 6 similarly presents the corresponding

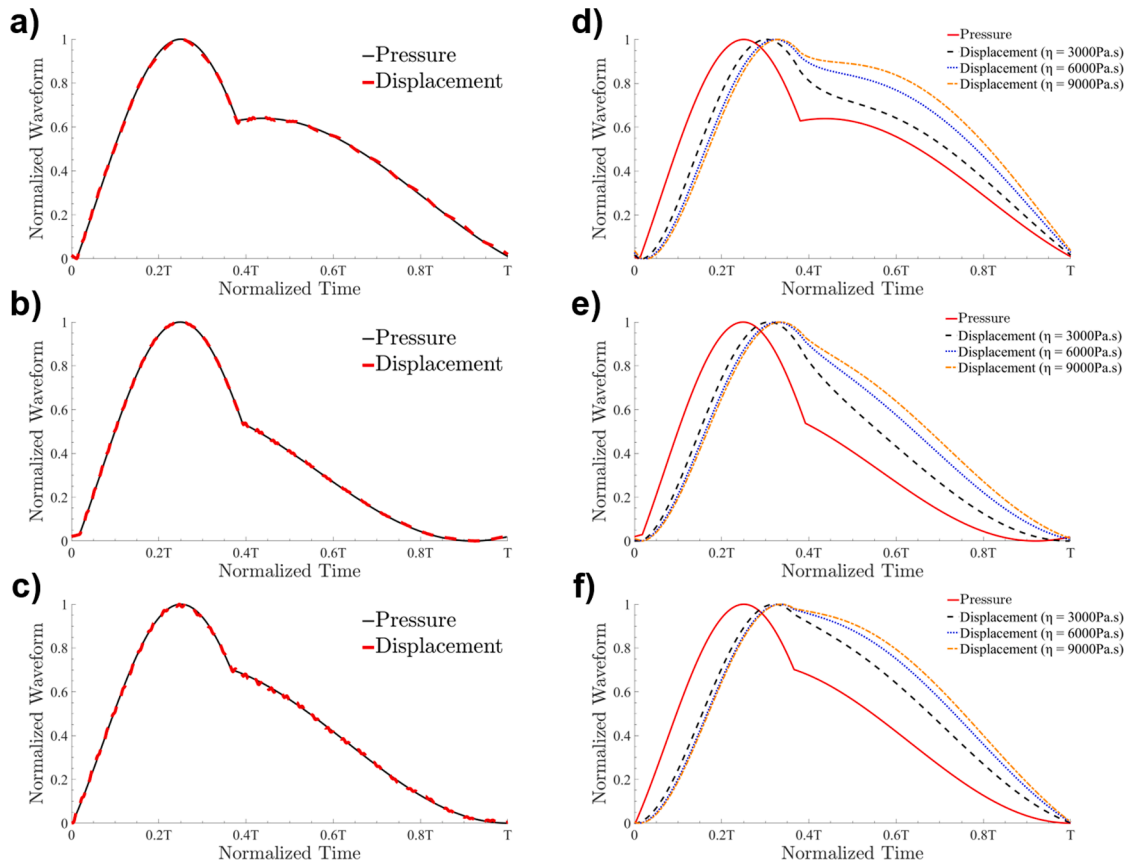


Fig. 4. Input pressure and (simulated) vessel wall displacement waveforms for elastic and viscoelastic wall configurations. The three input pressure cases (a,b,c), corresponding to low, medium, and high ω_1 , respectively, and their simulated elastic displacement waveforms. The same three pressure input cases (d,e,f) and the corresponding viscoelastic displacement waveforms (each simulated for three different wall viscosities). The results are for single-layer infinite tube models.

Table 2

Computed displacement-based IFs for single-layer and double-layer infinite tube models with linear, nonlinear and viscoelastic behavior.

Wall Material	Single-Layer		Double-Layer	
	ω_1	ω_2	ω_1	ω_2
Case 1 ($\omega_1 = 78.0$, $\omega_2 = 40.0$)				
Linear Elastic	78.0	40.0	78.0	40.0
Non-linear elastic	77.9	42.2	76.9	44.0
Viscoelastic Wall				
$\eta = 3000 \text{ Pa}\cdot\text{s}$	66.2	39.1	65.8	37.9
$\eta = 6000 \text{ Pa}\cdot\text{s}$	66.0	40.4	68.7	37.3
$\eta = 9000 \text{ Pa}\cdot\text{s}$	68.0	41.5	68.8	39.1
Case 2 ($\omega_1 = 103.5$, $\omega_2 = 52.8$)				
Linear Elastic	103.5	52.8	103.5	52.8
Non-linear elastic	103.2	52.9	102.0	54.2
Viscoelastic Wall				
$\eta = 3000 \text{ Pa}\cdot\text{s}$	121.0	44.6	119.2	44.6
$\eta = 6000 \text{ Pa}\cdot\text{s}$	113.1	43.9	112.5	44.5
$\eta = 9000 \text{ Pa}\cdot\text{s}$	107.7	39.8	105.9	42.2
Case 3 ($\omega_1 = 140.0$, $\omega_2 = 67.6$)				
Linear Elastic	140.0	67.6	140.0	67.6
Non-linear elastic	138.7	67.4	138.9	69.2
Viscoelastic Wall				
$\eta = 3000 \text{ Pa}\cdot\text{s}$	142.0	55.3	141.3	55.3
$\eta = 6000 \text{ Pa}\cdot\text{s}$	128.3	64.4	129.5	64.4
$\eta = 9000 \text{ Pa}\cdot\text{s}$	129.5	66.8	127.6	69.2

* All IFs (ω_1 , ω_2) are reported in units of beats per minutes (bpm). η denotes the vessel wall viscosity. Three different pressure waveforms cases (see Fig. 2) were used as the input.

Table 3

Computed displacement-based IFs for regular (straight) vessel model with linear, nonlinear and viscoelastic behavior (IF) parameters.

Wall Material	Displacement-Based		Pressure-Based		Error	
	ω_1	ω_2	ω_1	ω_2	ω_1	ω_2
Linear Elastic	108.5	54.8	108.5	54.8	0.00	0.00
Non-linear elastic	110.8	54.8	114.8	53	0.04	0.03
Viscoelastic Wall						
$\eta = 3000 \text{ Pa}\cdot\text{s}$	114.1	55.4	118.7	51.8	0.04	0.07
$\eta = 6000 \text{ Pa}\cdot\text{s}$	101.8	57.2	121.7	52.4	0.16	0.09
$\eta = 9000 \text{ Pa}\cdot\text{s}$	87.9	57.8	120.8	53.6	0.27	0.08

*Error is calculated based on the difference of displacement-based and pressure-based IFs normalized by pressure-based values $\left| \omega_i^{\text{press}} - \omega_i^{\text{disp}} \right| / \omega_i^{\text{press}}$, $i = 1, 2$. All IFs (ω_1 , ω_2) are reported in units of beats per minutes (bpm). η denotes the vessel wall viscosity.

flow, pressure, displacement amplitudes and the waveforms for the stenotic model. Table 4 presents values of ω_1 and ω_2 extracted from the displacement and pressure waveforms of the elastic, hyperelastic, and viscoelastic cases of the stenotic and aneurysmal vessel models.

4. Discussion

In this study, we examined the effects of vessel wall mechanics and irregular wall geometries on the accuracy of IFs extracted from displacement waveforms (which can be measured non-invasively) compared with the IFs extracted from the original pressure waveform (which requires invasive measurements). Employing a computational

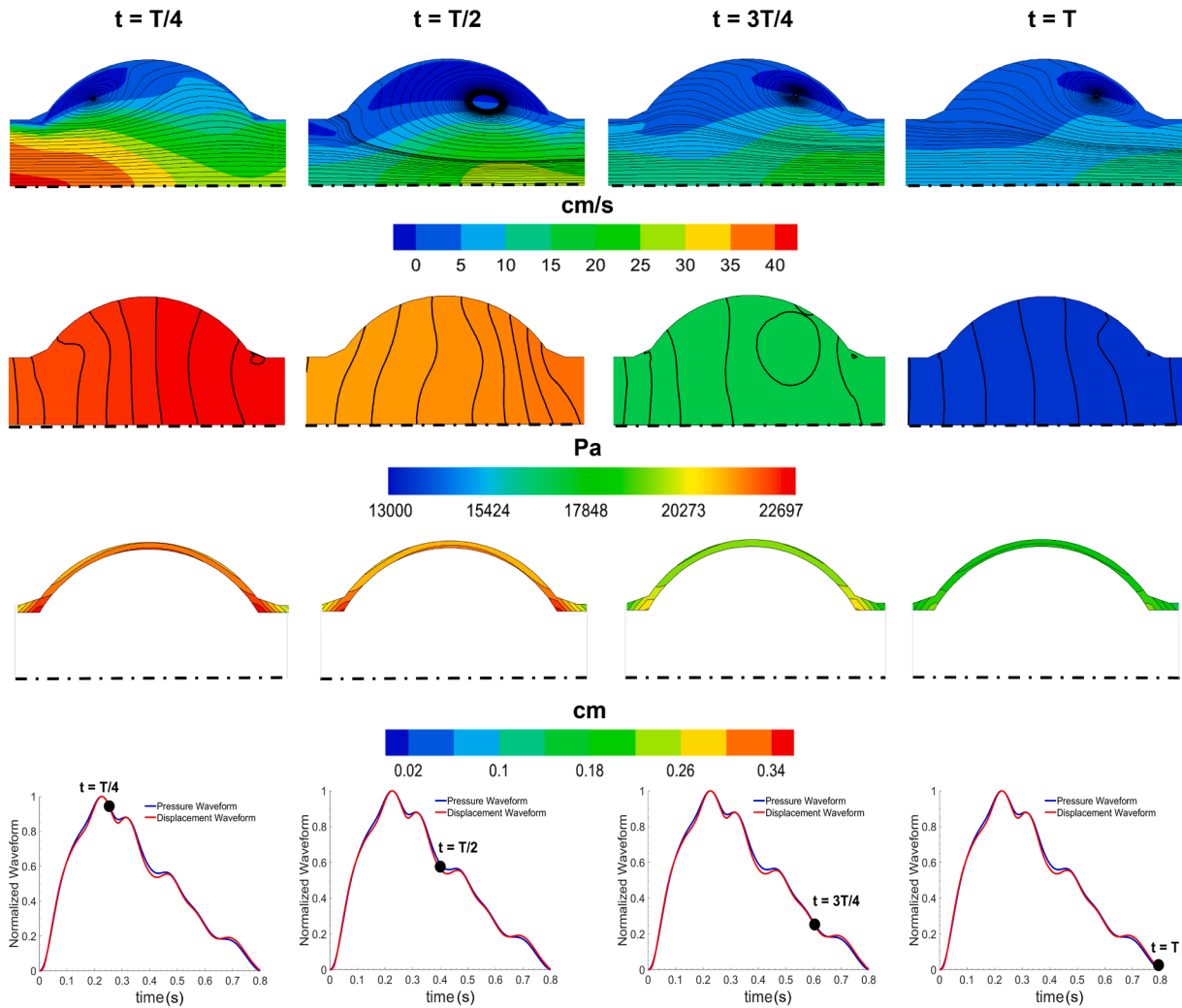


Fig. 5. Spatial distributions of fluid and solid behavior in the elastic aneurysmal model. (First row) Flow velocity amplitudes with streamlines overlaid, (second row) pressure distribution contours, (third row) vessel wall displacement contours at various times during a cardiac cycle and (fourth row) the normalized pressure and vessel wall displacement waveforms on top of the bulge.

FSI approach, we generated displacement waveforms corresponding to linear elastic, nonlinear elastic and viscoelastic vessel wall assumptions, and then extracted their corresponding IFs. For elastic vessel walls, we found that displacement-based IFs were almost identical to pressure-based IFs in all cases (a maximum error of 2%). For the non-linear elastic and viscoelastic vessel walls, we found non-negligible disagreements between the displacement-based IFs and pressure-based IFs, especially in the presence of geometrical abnormalities.

Our theoretical analysis of displacement-based IFs in linear viscoelastic solids indicates that viscoelasticity introduces an error between IFs extracted from displacement waveforms with those extracted from the pressure waveforms. As degree of viscoelasticity decreases, the discrepancy between displacement-based IFs and pressure-based IFs approaches zero. Indeed, the corresponding numerical simulations of this study on the infinite tube model demonstrates that relative error associated with the displacement-based IFs extracted from single-layer and double-layer wall models is negligible (see Table 2) for both linear and nonlinear elastic walls. This shows that elastic nonlinearity of a vessel wall does not affect the accuracy of (non-invasive) displacement-based IFs. As predicted by the theoretical analysis, the viscoelasticity increases the displacement-based IF error significantly (Table 2). According to our simulations, such errors vary nonlinearly with increasing viscoelasticity.

Similarly, for the finite tube models (Table 3), the errors between

pressure-based and displacement-based IFs are negligible in all elastic wall cases but significant in viscoelastic walls. This is physiologically relevant since the walls of large and medium-sized vessels exhibit a high degree of linear elasticity (Armentano et al., 1995; Fung, 2013; Learoyd and Taylor, 1966; Tucker et al., 2017). In the finite straight vessel cases (Table 3), non-linear elastic (hyperelastic) behavior of a vessel wall does not seem to generate a considerable effect on the accuracy of displacement-based IFs (maximum errors of 4%). Although this appears to be in line with previous findings which have suggested that a hyperelastic vessel wall assumption leads to small differences in the flow structure compared to the linear elastic case (Bilgi and Atalik, 2020), we find that, in the presence of geometric abnormalities such as stenosis and aneurysm (Table 4), these differences are no longer small (maximum errors approaching 11%, i.e., comparable to certain viscoelastic cases). Indeed, the viscoelastic wall properties result in significant differences between displacement-based and pressure-based IFs in all considered configurations (Tables 2–4). Such disagreement is more pronounced in ω_1 (a maximum error of 27%, corresponding to a straight viscoelastic wall) and less pronounced in the computation of ω_2 (a maximum error of 22%, corresponding to an aneurysmal viscoelastic wall). Since ω_1 is related to the systolic phase, the higher error is physiologically consistent with previously published findings that suggest the viscous effect is mainly developed during systole (Armentano et al., 1995). These results are also consistent with previous studies related to the effect of wall

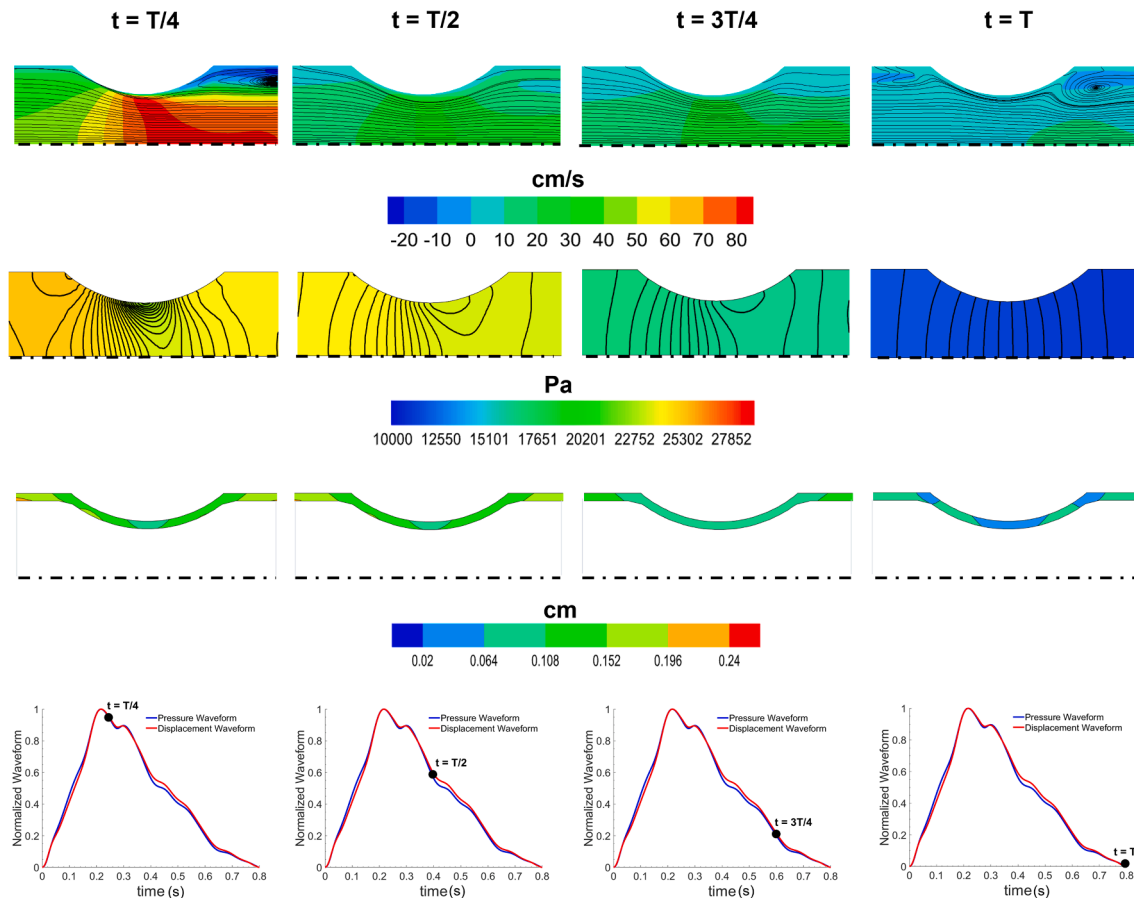


Fig. 6. Spatial distributions of fluid and solid behavior in the elastic stenotic model. (First row) Flow velocity amplitudes with streamlines overlaid, (second row) pressure distribution contours, (third row) vessel wall displacement contours at various times during a cardiac cycle and (fourth row) the normalized pressure and vessel wall displacement waveforms at the narrowest section of stenosis.

Table 4

Computed displacement-based IFs for irregular (stenotic and aneurysmal) vessel models with linear, nonlinear and viscoelastic behavior.

Wall Material	Displacement-Based		Pressure-Based		Error	
	ω_1	ω_2	ω_1	ω_2	ω_1	ω_2
Stenosis Case						
Linear Elastic	125.9	48.8	125.0	49.4	0.01	0.02
Non-linear elastic	115.9	53.6	130.4	50.6	0.11	0.06
Viscoelastic Wall						
$\eta = 3000 \text{ Pa}\cdot\text{s}$	121.4	55.4	138.8	48.8	0.12	0.13
$\eta = 6000 \text{ Pa}\cdot\text{s}$	116.6	56.0	111.4	56.0	0.05	0.00
$\eta = 9000 \text{ Pa}\cdot\text{s}$	104.5	56.6	116.9	54.2	0.11	0.04
Aneurysm Case						
Linear Elastic	114.2	45.2	111.8	46.4	0.02	0.02
Non-linear elastic	109.3	49.9	114.7	46.3	0.05	0.08
Viscoelastic Wall						
$\eta = 3000 \text{ Pa}\cdot\text{s}$	129.5	52.4	137.3	44.6	0.06	0.17
$\eta = 6000 \text{ Pa}\cdot\text{s}$	128.6	53.6	153.3	44.0	0.16	0.22
$\eta = 9000 \text{ Pa}\cdot\text{s}$	127.4	54.2	114.8	54.2	0.11	0.00

*Error is calculated based on the difference of displacement-based and pressure-based IFs normalized by pressure-based values $\left| \omega_i^{\text{press}} - \omega_i^{\text{disp}} \right| / \omega_i^{\text{press}}, i = 1, 2$. All IFs (ω_1, ω_2) are reported in units of beats per minutes (bpm). η denotes the vessel wall viscosity.

mechanics on the accuracy of displacement-based wave intensity (Kang et al., 2019).

In order to expand the applicability of displacement-based IFs on some diseased conditions, we have considered two types of geometric abnormalities related to vascular diseases: aneurysm and stenosis. Figs. 5 and 6 present the spatial distributions of the flow, pressure and wall displacement in the aneurysmal and stenotic wall models. As expected, there are significant differences in the flow and pressure distributions between these two models; higher amplitudes for the velocity inside the narrowing section of the stenosis can be observed, corresponding to higher pressure distributions in this model. Contour plots of the wall displacement are also presented in the figures, where differences between displacement amplitudes of the two cases can be attributed to the corresponding differences in flow velocity magnitudes. We calculated IF variables based on the pressure and displacement waveforms at the top of the bulge of the aneurysm (largest diameter) and the narrowing section of the stenosis (smallest diameter). The maximum disagreement (over both IFs) between pressure-based and displacement-based IFs at other locations for the aneurysmal (resp. stenotic) models are 17% pre-bulge (resp. 11% pre-narrowing) and 16% post-bulge (resp. 9% post-narrowing) for all the different wall conditions. At the maximum bulge (resp. minimum stenotic diameter), the maximum error is 22% (resp. 13%), and so we have adopted this location for our analysis in order to consider the most extreme (largest disagreement) cases. For these diseased cases, our analysis has illustrated a good agreement

between the displacement-based and pressure-based IFs for the purely elastic and hyperelastic vessel walls, although there exist slight differences for the hyperelastic cases. For viscoelastic models applied to aneurysm and stenosis, the error grows in general in a nonlinear fashion similar to the straight vessel cases (Tables 3 and 4).

Ultimately, our results strongly support the application of non-invasively measured waveforms (e.g., wall displacement) for IF analysis. This is of practical value due to the recent and ongoing advancements in rapid, inexpensive, and non-invasive pulse waveform measurements (e.g., via smartphone cameras, infrared, wearable technologies, etc. (Pahlevan et al., 2017; Rastegar et al., 2020; Wang et al., 2018)). Our results are also valuable for the use of IF-based machine learning or artificial intelligence models, whose input could then potentially be provided by any arbitrary displacement-based measurement, thereby facilitating non-invasive and low-risk collection of larger training/testing datasets for big-data analysis.

5. Conclusion

Our results show that the displacement-based IFs for arteries demonstrating linear elastic behavior are almost identical to pressure-based IFs. This is clinically significant because displacement-based IFs can be measured non-invasively. The present study shows that, for large central arteries (e.g., carotids), the error between non-invasive waveform measurements (displacement-based) and invasive measurements

(pressure-based) is negligible. The results of this study ultimately suggest that, although employing displacement-based IFs introduce errors into IF analysis for vessels with viscoelastic behavior (which is exhibited mostly by smaller vessels), these errors are negligible for larger (primarily elastic) arteries, and hence may be an acceptable compromise in order to enable non-invasive measurements of IFs for broader use in clinical applications.

Declaration of Competing Interest

The authors declare the following financial interests/personal relationships which may be considered as potential competing interests: [NP holds equity in Avicena LLC and has consulting agreement with Avicena LLC. The other authors report no conflicts].

Acknowledgements

AA gratefully acknowledges Alfred E. Mann Innovation in Engineering Doctoral Fellowship support from the Alfred E. Mann Institute.

Sources of funding

This study was partially funded by American Heart Association (AHA) Career Development Award No. 20CDA35260167 to NP.

Appendix A. . Details of boundary conditions and computational model

The finite axisymmetric configurations considered in this work were discretized by four-node axisymmetric elements. A flow velocity waveform was applied to the vessel inlet as a boundary condition (source), and a constant normal traction of 10.5 mmHg was applied at the outlet of the outflow boundary model (Pahlevan et al., 2011) consisting of a flexible tube and a rigid tube with contraction, was applied to the vessel outlet (Fig. 2) to account for the effects of compliance, resistance, and wave reflections in the truncated downstream vasculature. The fluid and solid domains were coupled at the inner surface of the vessel wall and the edge of the fluid domain opposite the fluid–solid interface was defined as the axis of symmetry (see Fig. 2). The outer surface of the vessel wall was considered as a free boundary. The face of the vessel inlet and the rigid portion of the boundary model were considered as fixed. A time step of 2 ms was used for the temporal discretization. For the infinite tube, the model consisted of 2D four-node elements. Pressure waveforms reconstructed by the exact (known) IFs were applied to the inner surface of the vessel wall. The outer surface of the vessel wall was considered a free boundary. The interior of the vessel was filled with solid elements of negligible Young's modulus so that the center of the model remained fixed.

An Arbitrary Lagrangian-Eulerian (ALE) finite element analysis was applied to all cases, and the corresponding linearized systems of equations were solved using direct solution techniques (Bathe et al., 1997). The final times of the simulations were chosen such that oscillatory steady-state behavior was achieved (typically, at least five cardiac cycles). Convergence studies in both space and time were performed to determine appropriate spatial and temporal discretization that were within 3% error (with the finest grids) in terms of capturing displacement waveforms. We have employed $N = 10000$ elements in the fluid domain and $N = 1200$ elements in the solid domain for the straight vessel simulations; $N = 10900$ elements in the fluid domain and $N = 1412$ elements in the solid domain for the aneurysmal vessel simulations; and $N = 10440$ elements in the fluid domain and $N = 1322$ elements in the solid domain for the stenotic vessel simulations. The commercial package ADINA 9.6 (ADINA R&D, Inc., MA) was used to run all simulations in the present work.

Appendix B. . Governing Equation: Fluid dynamics of blood flow

To obtain the pressure and flow fields in the fluid domain of the finite axisymmetric models, the continuity and momentum equations for the incompressible Newtonian fluid (the Navier-Stokes equations) that are employed in this work are given by

$$\begin{cases} \nabla \cdot \mathbf{v} = 0, \\ \rho_f \dot{\mathbf{v}} + \rho_f (\mathbf{v} \cdot \nabla) \mathbf{v} - \nabla \cdot \mathbf{T}_f = \mathbf{f} = 0, \\ \mathbf{T}_f = -p\mathbf{I} + \mu(\nabla \mathbf{v} + \nabla \mathbf{v}^T), \end{cases} \quad (\text{A1})$$

where \mathbf{I} is the identity tensor, \mathbf{v} is the fluid velocity, p is the static pressure, ρ_f is the fluid density, μ is the dynamic viscosity, \mathbf{f} is the body force, and \mathbf{T}_f is the fluid stress tensor. Assuming a no-slip boundary, the corresponding kinematic and dynamic coupling conditions at the fluid–solid interface are given respectively by

$$\mathbf{v} = \dot{\mathbf{u}}_s, \quad (\text{A2})$$

$$\mathbf{T}_f \mathbf{n} = \mathbf{T}_s \mathbf{n}, \quad (\text{A3})$$

where $\dot{\mathbf{u}}_s$ is the solid wall velocity (given by the solid solver as described in what follows), \mathbf{T}_s is the solid stress tensor, and \mathbf{n} is the normal direction to the interface.

Governing Equation: Solid dynamics of vessel wall displacement

Vessel wall motion was calculated using the Lagrangian form of the momentum balance equations given by

$$\frac{\partial \mathbf{T}_s}{\partial \mathbf{x}} + \mathbf{F} = \rho_s \ddot{\mathbf{u}}_s \quad (\text{A4})$$

where \mathbf{x} is the position of a material point, \mathbf{F} is an external force, ρ_s is the vessel wall density, and $\ddot{\mathbf{u}}_s$ is the solid wall acceleration. The stress tensor \mathbf{T}_s depends on the material properties of the vessel wall (linear elastic, nonlinear elastic, or viscoelastic)

References

- Aghilinejad, A., Amlani, F., King, K.S., Pahlevan, N.M., 2020. Dynamic Effects of Aortic Arch Stiffening on Pulsatile Energy Transmission to Cerebral Vasculature as a Determinant of Brain-Heart Coupling. *Sci. Rep.* 10, 1–12.
- Aghilinejad, A., Amlani, F., Liu, J., Pahlevan, N.M., 2021. Accuracy and applicability of non-invasive evaluation of aortic wave intensity using only pressure waveforms in humans. *Physiol. Meas.*
- Alavi, R., Dai, W., Amlani, F., Rinderknecht, D.G., Kloner, R.A., Pahlevan, N.M., 2021. Scalability of cardiovascular intrinsic frequencies: Validations in preclinical models and non-invasive clinical studies. *Life Sci.* 284, 119880. <https://doi.org/10.1016/j.lfs.2021.119880>.
- Alavi, R., Dai, W., Kloner, R.A., Pahlevan, N.M., 2019. A Hybrid Artificial Intelligence-Intrinsic Frequency Method for Instantaneous Detection of Acute Myocardial Infarction. *Circulation* 140, A12573–A12573.
- Alavi, R., Dai, W., Kloner, R.A., Pahlevan, N.M., 2020. A Hybrid Artificial Intelligence-Intrinsic Frequency Method for Instantaneous Determination of Myocardial Infarct Size. *Circulation* 142, A15899–A15899.
- Amabili, M., Balasubramanian, P., Breslavsky, I., Ferrari, G., Tubaldi, E., 2018. Viscoelastic characterization of woven Dacron for aortic grafts by using direction-dependent quasi-linear viscoelasticity. *J. Mech. Behav. Biomed. Mater.* 82, 282–290.
- Armentano, R.L., Barra, J.G., Levenson, J., Simon, A., Pichel, R.H., 1995. Arterial wall mechanics in conscious dogs: assessment of viscous, inertial, and elastic moduli to characterize aortic wall behavior. *Circ. Res.* 76 (3), 468–478.
- Bilgi, C., Atalik, K., 2020. Effects of blood viscoelasticity on pulsatile hemodynamics in arterial aneurysms. *J. Nonnewton. Fluid Mech.* 279, 104263. <https://doi.org/10.1016/j.jnnfm.2020.104263>.
- Cooper, L.L., Rong, J., Pahlevan, N.M., Rinderknecht, D.G., Benjamin, E.J., Hamburg, N. M., Vasan, R.S., Larson, M.G., Gharib, M., Mitchell, G.F., Intrinsic Frequencies of Carotid Pressure Waveforms Predict Heart Failure Events: The Framingham Heart Study. *Hypertension*, HYPERTENSIONAHA. 120.15632.
- Fung, Y.-C., 2013. *Biomechanics: mechanical properties of living tissues*. Springer Science & Business Media.
- Gasser, T.C., Ogden, R.W., Holzapfel, G.A., 2006. Hyperelastic modelling of arterial layers with distributed collagen fibre orientations. *J. R. Soc. Interface* 3 (6), 15–35.
- Holzapfel, G.A., Gasser, T.C., Stadler, M., 2002. A structural model for the viscoelastic behavior of arterial walls: continuum formulation and finite element analysis. *European J. Mech.-A/Solids* 21 (3), 441–463.
- Holzapfel, G.A., Sommer, G., Gasser, C.T., Regitnig, P., 2005. Determination of layer-specific mechanical properties of human coronary arteries with nonatherosclerotic intimal thickening and related constitutive modeling. *American J. Physiol.-Heart Circulatory Physiol.* 289 (5), H2048–H2058.
- Kang, J., Aghilinejad, A., Pahlevan, N.M., Borazjani, I., 2019. On the accuracy of displacement-based wave intensity analysis: Effect of vessel wall viscoelasticity and nonlinearity. *PLoS ONE* 14 (11), e0224390.
- Learoyd, B.M., Taylor, M.G., 1966. Alterations with age in the viscoelastic properties of human arterial walls. *Circ. Res.* 18 (3), 278–292.
- Lin, C.-Y., 2020. Alternative form of standard linear solid model for characterizing stress relaxation and creep: including a novel parameter for quantifying the ratio of fluids to solids of a viscoelastic solid. *Front. Mater.* 7, 11.
- Liu, J., Pahlevan, N.M., 2021. The underlying mechanism of inter-site discrepancies in ejection time measurements from arterial waveforms and its validation in the Framingham Heart Study. *American Journal of Physiology-Heart and Circulatory Physiology*. 321 (1), H135–H148.
- Martins, P., Natal Jorge, R., Ferreira, A., 2006. A comparative study of several material models for prediction of hyperelastic properties: Application to silicone-rubber and soft tissues. *Strain* 42, 135–147.
- Miller, J.C., Shepherd, J., Rinderknecht, D., Cheng, A.L., Pahlevan, N.M., Jefferies, J.L., 2020. Proof-of-concept for a non-invasive, portable, and wireless device for cardiovascular monitoring in pediatric patients. *PLoS ONE* 15 (1), e0227145.
- Mogadam, E., Shavelle, D.M., Giesler, G.M., Economides, C., Lidia, S.P., Duquette, S., Matthews, R.V., Pahlevan, N.M., 2020. Intrinsic frequency method for instantaneous assessment of left ventricular-arterial coupling after transcatheter aortic valve replacement. *Physiol. Meas.* 41 (8), 085002. <https://doi.org/10.1088/1361-6579/aba67f>.
- Mynard, J.P., Smolich, J.J., 2016. Novel wave power analysis linking pressure-flow waves, wave potential, and the forward and backward components of hydraulic power. *American Journal of Physiology-Heart and Circulatory Physiology* 310 (8), H1026–H1038.
- Pahlevan, N.M., Alavi, R., Ramos, M., Hindoyan, A., Matthews, R.V., 2020. An Artificial Intelligence Derived Method for Instantaneous Detection of Elevated Left Ventricular End Diastolic Pressure. *Circulation* 142, A16334–A16334.
- Pahlevan, N.M., Amlani, F., Hossein Gorji, M., Hussain, F., Gharib, M., 2011. A physiologically relevant, simple outflow boundary model for truncated vasculature. *Ann. Biomed. Eng.* 39 (5), 1470–1481.
- Pahlevan, N.M., Gharib, M., 2011. Low pulse pressure with high pulsatile external left ventricular power: influence of aortic waves. *J. Biomech.* 44 (11), 2083–2089.
- Pahlevan, N.M., Matthews, R.V., 2019. Cardiac Triangle Mapping: A New Systems Approach for Noninvasive Evaluation of Left Ventricular End Diastolic Pressure. *Fluids* 4 (1), 16. <https://doi.org/10.3390/fluids4010016>.
- Pahlevan, N.M., Rinderknecht, D.G., Tavallali, P., Razavi, M., Tran, T.T., Fong, M.W., Kloner, R.A., Csete, M., Gharib, M., 2017. Noninvasive iPhone measurement of left ventricular ejection fraction using intrinsic frequency methodology. *Crit. Care Med.* 45 (7), 1115–1120.
- Pahlevan, N.M., Tavallali, P., Rinderknecht, D.G., Petrusek, D., Matthews, R.V., Hou, T. Y., Gharib, M., 2014. Intrinsic frequency for a systems approach to haemodynamic waveform analysis with clinical applications. *J. R. Soc. Interface* 11 (98), 20140617. <https://doi.org/10.1098/rsif.2014.0617>.
- Parker, K.H., 2009. An introduction to wave intensity analysis. *Med. Biol. Eng. Comput.* 47 (2), 175–188.
- Payne, S., Year A two-layer model of the static behaviour of blood vessel walls. In *The 26th Annual International Conference of the IEEE Engineering in Medicine and Biology Society*.
- Petrusek, D., Pahlevan, N.M., Tavallali, P., Rinderknecht, D.G., Gharib, M., 2015. Intrinsic frequency and the single wave biopsy: Implications for insulin resistance. *J. Diabetes Sci. Technol.* 9 (6), 1246–1252.
- Qiu, J., Li, F.-F., 2019. Identification of Viscoelastic Constitutive Parameters of a Cell Based on Fluid-Structure Coupled Finite Element Model and Experiment. *Mathematical Problems in Engineering* 2019.
- Rastegar, S., Gholamhosseini, H., Lowe, A., 2020. Non-invasive continuous blood pressure monitoring systems: current and proposed technology issues and challenges. *Phys. Eng. Sci. Med.* 43 (1), 11–28.
- Reymond, P., Merenda, F., Perren, F., Rüfenacht, D., Stergiopoulos, N., 2009. Validation of a one-dimensional model of the systemic arterial tree. *American J. Physiol.-Heart Circulatory Physiology* 297 (1), H208–H222.
- Rinderknecht, D., De Balasy, J.M., Pahlevan, N.M., 2020. A wireless optical handheld device for carotid waveform measurement and its validation in a clinical study. *Physiol. Meas.* 41 (5), 055008. <https://doi.org/10.1088/1361-6579/ab7b3f>.
- Simon, A., Levenson, J., 2001. Effect of hypertension on viscoelasticity of large arteries in humans. *Curr. Hypertens. Rep.* 3 (1), 74–78.
- Stefanadis, C., Dernellis, J., Vlachopoulos, C., Tsoufis, C., Tsimis, E., Toutouzas, K., Pitsavos, C., Toutouzas, P., 1997. Aortic function in arterial hypertension determined by pressure-diameter relation: effects of diltiazem. *Circulation* 96 (6), 1853–1858.
- Tavallali, P., Hou, T.Y., Rinderknecht, D.G., Pahlevan, N.M., 2015. On the convergence and accuracy of the cardiovascular intrinsic frequency method. *R. Soc. Open Sci.* 2 (12), 150475. <https://doi.org/10.1098/rsos.150475>.
- Tavallali, P., Razavi, M., Pahlevan, N.M., 2018. Artificial intelligence estimation of carotid-femoral pulse wave velocity using carotid waveform. *Sci. Rep.* 8, 1–12.
- Tucker, W.D., Arora, Y., Mahajan, K., 2017. Anatomy, blood vessels.
- Wang, G., Atef, M., Lian, Y., 2018. Towards a continuous non-invasive cuffless blood pressure monitoring system using PPG: Systems and circuits review. *IEEE Circuits Syst. Mag.* 18 (3), 6–26.
- Wang, Z., Wood, N.B., Xu, X.Y., 2015. A viscoelastic fluid-structure interaction model for carotid arteries under pulsatile flow. *Int. J. Numerical Methods Biomed. Eng.* 31 (5), e02709. <https://doi.org/10.1002/cnm.2709>.
- Warriner, R.K., Johnston, K.W., Cobbald, R.S.C., 2008. A viscoelastic model of arterial wall motion in pulsatile flow: implications for Doppler ultrasound clutter assessment. *Physiol. Meas.* 29 (2), 157–179.
- Young, D.F., Tsai, F.Y., 1973. Flow characteristics in models of arterial stenoses—I. Steady flow. *J. Biomech.* 6 (4), 395–410.
- Bathe, K.J., Zhang, H., Zhang, X., 1997. Some advances in the analysis of fluid flows. *Comput. Struct.* 64 (5-6), 909–930.